On jet-wake flame stabilization in scramjet: A LES/RANS study from chemical kinetic and fluid-dynamical perspectives

Kun Wu [a], Peng Zhang [b], Xuejun Fan [a,c,*]

[a] *State Key Laboratory of High Temperature Gas Dynamics, Institute of Mechanics, Chinese Academy of Sciences, Beijing, 100190, People's Republic of China*
[b] *Department of Mechanical Engineering, the Hong Kong Polytechnic University, Hung Hom, Kowloon, Hong Kong*
[c] *School of Engineering Sciences, University of Chinese Academy of Sciences, Beijing 100049, People's Republic of China*

ARTICLE INFO

ABSTRACT

A three-dimensional hybrid LES (Large Eddy Simulation)/RANS (Reynolds-averaged Navier–Stokes) study dedicated to understanding the jet-wake flame stabilization under high inflow stagnation temperature in a hydrogen-fueled dual-mode scramjet was presented in this paper. The computational method features a finite-rate PaSR (Partially Stirred Reactor) turbulent combustion model with a detailed hydrogen reaction mechanism. The simulation results agreed well with the experimental results on overall characteristics of the jet-wake flame stabilization mode. Furthermore, quantitatively satisfactory predictions were attained for wall pressures. From the chemical kinetic perspective, the jet-wake flame stabilization can be divided into two regions. In the upstream region, both premixed- and non-premixed combustion are responsible for radical production, and the former produces more heat release. In the downstream region, turbulent non-premixed combustion dominates the flame stabilization. From the fluid dynamic perspective, the premixed flame is sustained by the counter-rotating vortex pair in the leeward side of the jet plume, which creates a local region with enhanced fuel/air mixing and reduced local flow velocity. Non-premixed combustion is found in the leeward side periphery of the fuel jet.

© 2021 Elsevier Masson SAS. All rights reserved.

1. Introduction

Hypersonic propulsion at flight Mach number (Ma_f) above 5 is desirable for space launch, military and passenger transportations [1]. Dual-mode scramjet engines have been identified as the promising candidate for practical propulsion to cover this flight corridor ($Ma_f = 4 \sim 7$). Generally, a dual-mode scramjet engine needs to be accelerated to $Ma_f = 3 \sim 4$ before it can be started, and then operates in the thermally chocked ramjet mode at moderate flight Mach numbers ($Ma_f = 4 \sim 5$), then enters the scramjet mode as it accelerates to $Ma_f = 6 \sim 7$, when the pre-combustion shock train becomes so weak that the isolator exit flow reaches supersonic. Consequently, the dual-mode scramjet poses a prominent challenge in flame stabilization because the incoming flow temperature is insufficiently high to sustain consistent auto-ignition [1]. Therefore, several flameholding strategies have been applied in supersonic combustors, such as transverse injection [2], strut injection [3], and cavity flame holder [4,5]. Among these, wall cavity is the most prevailing one owing to its wide stabilization regime and low total pressure loss [6].

In a typical cavity-assisted dual-mode scramjet, Micka and Driscoll [7] experimentally identified two distinct statistically stable flame stabilization modes. In the cavity mode at relatively low inflow stagnation temperature (T_0), the flame is anchored at the leading edge of the cavity shear layer. In the jet-wake mode at relatively high T_0, the flame is stabilized in the wake of the fuel jet. The jet-wake mode bears certain similarities with the canonical fuel jet-in-cross-flow (JICF) configuration [8]. Many previous studies [9,10] on reacting JICF at a flow velocity of O(10) m/s found that flame extinction occurred when the cross-flow velocity was increased to O(100) m/s. At a sufficiently high stagnation temperature ($T_0 = 1290$ K), hydrogen/ethylene combustion was stabilized in supersonic flow in a shock tube experiment by Ben-Yakar et al. [11]. Gamba et al. [2] experimentally investigated the hydrogen jet flame in supersonic cross-flow at $T_0 = 1400$ K and found that the flame was influenced by the momentum flux ratio J of the fuel jet and the cross-flow. The flame is lifted and stabilized in the jet wake at low J, and it is anchored at the upstream recirculation zone and attached to the wall within the boundary layer at high J.

In a real scramjet engine, the heat release from combustion could alter the inflow condition through the upstream-propagating

* Corresponding author at: State Key Laboratory of High Temperature Gas Dynamics, Institute of Mechanics, Chinese Academy of Sciences, Beijing, 100190, People's Republic of China.
E-mail address: xfan@imech.ac.cn (X. Fan).
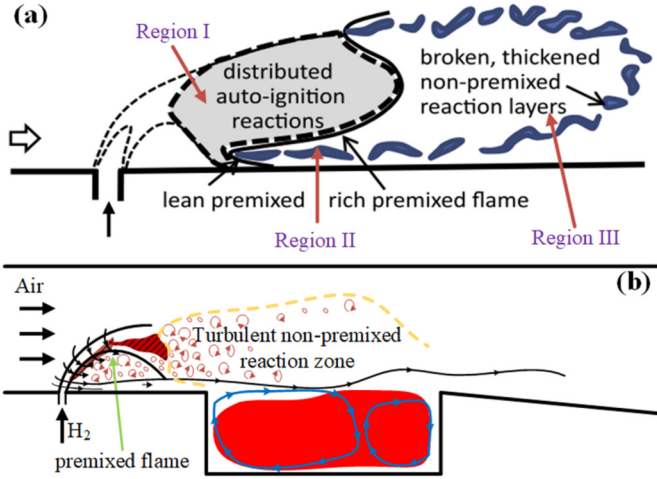
Fig. 1. Schematic of the jet-wake flame stabilization mode (a) fueled with blended $C_2H_4+H_2$ [12] and (b) with contracted auto-ignition region.

backpressure, which in turn modulates the combustion characteristics in the downstream. In the experiments of Micka et al. [12] on the jet-wake flame stabilization mode in a dual-mode scramjet at high $T_0 = 1390$ K with blended hydrogen-ethylene fuel jet, they identified three regions of flame stabilization, as sketched in Fig. 1(a), such as a lift-off autoignition controlled region (region I), a lifted flame base characterized by a premixed flame with intensive heat release (region II), and downstream turbulent non-premixed reaction zones (region III).

Besides the well resolved formaldehyde and CH planar laser induced fluorescence (CH-PLIF) in experiments [12], the rationality of inferring autoignition to occur in region I was based on ignition delay estimation in homogeneous reactor. Non-uniformities in equivalence ratio, temperature, and flow velocity have not been accounted for in the inference. Furthermore, Micka et al.'s three-region flame stabilization mechanism was based on hydrogen/ethylene mixture at a fixed blending ratio (50%-50% in volume fraction), so that the influence of fuel reactivity was to be determined. It is a reasonable hypothesis that the reduced chemical induction time will contract region I and move region II to upstream, as illustrated in Fig. 1(b). It is however experimentally challenging to verify this hypothesis due to the extremely short lifetime of hydrogen autoignition precursors such as HO_2. Similar operation conditions for the same scramjet were also numerically studied by Fureby et al. [13] and Koo et al. [14]. The former study was concerned more with the capability of large-eddy simulation (LES) on reacting flow prediction compared to Reynolds-averaged Navier-Stokes simulation (RANS), and the latter employed the experimental data for numerical validation of the turbulence combustion model. Consequently, the flame stabilization mechanism especially for the jet-wake stabilization is still insufficiently understood.

Based on the above considerations, we aimed to employ the hybrid LES/RANS simulation to investigate the jet-wake flame stabilization mode observed by Micka and Driscoll [7] in a hydrogen-fueled dual-mode scramjet. The characteristics of the jet-wake flame mode will be analyzed from the dual aspects of chemical kinetics and fluid dynamics, and the underlying physics governing the flame stabilization will be further elucidated. The present paper is organized as follows: the next section is devoted to the problem description and computational specifications. After a comprehensive numerical validation, a phenomenological description of the jet-wake flame stabilization mode is presented. Then, the flame stabilization characteristics are qualitatively illustrated and further quantified in terms of representative engine performance metrics. Subsequently, the obtained results are used to reveal the

flame structure and stabilization mechanism. Finally, the concluding remarks are presented.

2. Problem description and computational methodology

2.1. Problem description

The University of Michigan's Supersonic Combustion Facility is a laboratory-scale direct-connect dual-mode scramjet combustor which was designed to simulate flight Mach numbers up to 5.5. A series of experiments were conducted in a wide range of inflow stagnation temperature, equivalence ratio, and fuel mixture blending ratio. Experiment data was gathered using various measurement techniques such as wall static pressure and OH* luminosity for hydrogen fueled combustion. Because of its well-designed experiments along with comprehensive measurements, the facility was adopted by the present numerical simulation to peruse the flame stabilization mechanism.

As shown in Fig. 2, the incoming vitiated air supplied by a two-dimensional nozzle consists of 64.2% N_2, 24.7% O_2, and 11.1% H_2O in mass fraction, and it has a stagnation pressure $p_0 = 590$ KPa and temperature $T_0 = 1400$ K at Mach number 2.2. The constant area isolator has a height (H) of 25.4 mm, a width (W) of 38.1 mm, and a length of 358 mm. Room-temperature hydrogen at $p_0 = 755$ kPa is injected normally to the crossflow through a sonic injection port, which is 2.49 mm in diameter (D) and flush installed at 44.5 mm upstream of the cavity. The rectangular wall cavity is 50.8 mm long, 12.7 mm deep, and spans the entire width of the combustor. The expansion section behind the cavity is 359 mm long with a 4° divergence angle.

In the experiment of Micka and Driscoll [7], a very small amount (5%) of pilot fuel was injected directly into the cavity through three spanwise distributed orifices of 1.19 mm in diameter, which were mounted on the cavity rear wall and 3.8 mm above the floor. The overall equivalence ratio of the experiment ϕ_g equals to 0.25. However, the main fuel upstream the cavity has an dominant mass flow ratio of 95%, implying the negligible influence of the pilot fuel on flame stabilization [7]. Consequently, the fuel injection in the cavity is neglected in the simulation, and instead an overall equivalence ratio $\phi_g = 0.24$ is specified. By using such a simplification, we can avoid the unnecessary complexity caused by the increased computational overhead for clustering grid points to the cavity fuel injectors. Further justification of the simplification will be seen in the following section, where the computational results are compared with the experimental results.

2.2. Physical modeling and numerical algorithms

2.2.1. Governing equations

The governing equations are derived from the fully compressible reactive Navier-Stokes equations including species conservation equations. Correspondingly, the Favre-averaged three-dimensional unsteady governing equations are given as follows:

$$\frac{\partial \overline{\rho}}{\partial t} + \frac{\partial \overline{\rho}\tilde{u}_j}{\partial x_j} = 0 \tag{1}$$

$$\frac{\partial \overline{\rho}\tilde{u}_j}{\partial t} + \frac{\partial}{\partial x_j}\left[\overline{\rho}\tilde{u}_i\tilde{u}_j + \overline{p}\delta_{ij} - \overline{\tau}_{ij} + \tau_{ij}^{sgs}\right] = 0 \tag{2}$$

$$\frac{\partial \overline{\rho}\tilde{E}}{\partial t} + \frac{\partial}{\partial x_j}\left[(\overline{\rho}\tilde{E} + \overline{p})\tilde{u}_j + \overline{q}_j - \tilde{u}_i\overline{\tau}_{ij} + H_j^{sgs} + \sigma_j^{sgs}\right] = \overline{\dot{\omega}}_T \tag{3}$$

$$\frac{\partial \overline{\rho}\tilde{Y}_k}{\partial t} + \frac{\partial}{\partial x_j}\left[\overline{\rho}\tilde{u}_j\tilde{Y}_k - \overline{\rho}D_{km}\frac{\partial \tilde{Y}_k}{\partial x_j} + \Upsilon_{j,k}^{sgs}\right] = \overline{\dot{\omega}}_k$$

$$k = 1, \ldots, N_s \tag{4}$$
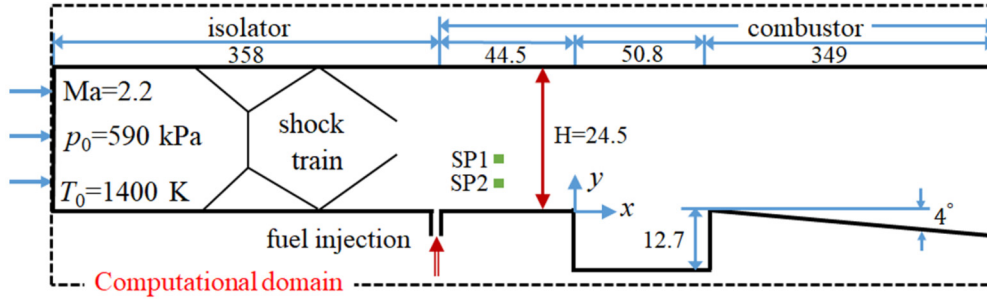
Fig. 2. Geometry and dimensions of the dual-mode scramjet combustor [7]. SP1 and SP2 denote sampling points at locations ($x = -12.7$, $y = 6.35$) and ($x = -12.7$, $y = 12.7$) on the combustor central plane, respectively (all units in mm). The computational domain is enclosed by the dot lines.

in which "−" and "∼" represent spatial and Favre filtered quantities, respectively. ρ is the density, $u_j (j = 1, 2, 3)$ the velocity components, p the pressure, τ_{ij} $(i, j = 1, 2, 3)$ the viscous stress tensor. The total energy represents $E = h_s - p/\rho + 1/2u_j^2$ with h_s being the sensible enthalpy, and q_j $(j = 1, 2, 3)$ is the heat flux components. The Y_k $(k = 1, 2, \ldots, N_S)$ denotes mass fraction of the kth species, D_{km} the mixture-averaged mass diffusivity of species k, which is obtained by using the modified Wilke's law. Furthermore, $\dot{\omega}_k$ is the instantaneous production rate of species k, and $\dot{\omega}_T$ the heat production rate due to chemical reaction.

Following the thermally perfect gas assumption, the thermodynamic properties are calculated by using the NIST-JANAF database [15]. The thermodynamic state variables are related via the filtered equation of state $\overline{p} = \overline{\rho} R \tilde{T}$, where T is the temperature, $R = \sum_{k=1}^{N_S} Y_k R_u / MW_k$ the gas constant of the mixture, MW_k the species molecular weight, and R_u the universal gas constant. The molecular viscosity for individual species obeys Sutherland's law, and the thermal conductivity and species mass diffusivities are calculated from the viscosity by assuming constant Prandtl ($Pr = 0.7$) and Schmidt numbers ($Sc = 0.7$), respectively.

2.2.2. Turbulence and combustion modeling

The subgrid stress tensor τ_{ij}^{sgs} can be expressed as

$$\tau_{ij}^{sgs} = -2\overline{\rho} \upsilon_t \left(\tilde{S}_{ij} - \frac{1}{3} \tilde{S}_{kk} \delta_{ij} \right) + \frac{2}{3} k^{sgs} \delta_{ij} \quad (5)$$

here $\tilde{S}_{ij} = \frac{1}{2} (\frac{\partial u_i}{\partial x_j} + \frac{\partial u_j}{\partial x_i})$, k^{sgs} is the unresolved turbulent kinetic energy, υ_t is the eddy viscosity given by an approximate turbulence model. H_j^{sgs} and σ_j^{sgs} in the energy equation are lumped together as:

$$H_j^{sgs} + \sigma_j^{sgs} = -\frac{\overline{\rho} \upsilon_t}{Pr_t} \left(\frac{\partial h_s}{\partial x_j} + \tilde{u}_j \frac{\partial \tilde{u}_i}{\partial x_j} + \frac{\partial k^{sgs}}{\partial x_j} \right) \quad (6)$$

The subgrid species flux $\Upsilon_{j,k}^{sgs}$ is calculated with the gradient diffusion assumption,

$$\Upsilon_{j,k}^{sgs} = -\frac{\overline{\rho} \upsilon_t}{Sc_t} \frac{\partial \tilde{Y}_k}{\partial x_j} \quad (7)$$

in which the turbulent Prandtl and Schmidt numbers Pr_t and Sc_t are 0.9 and 0.72, respectively.

Although its applicability has been extensively demonstrated, the wall-resolved LES is still expensive for full-scale simulation of industrial supersonic combustors, especially at high Reynolds numbers [16,17]. Consequently, a hybrid LES/RANS approach is employed in the present simulation as a compromise of computational accuracy and the daunting computational cost of wall-resolved LES of realistic scramjet combustor [18]. In this approach, the attached wall boundary layer is fully covered by the background RANS model of one-equation Spalart-Allmaras model (S-A)

[19] and transits to LES away from the wall into the core flow, constituting the Improved Delayed Detached-Eddy Simulation [20] (IDDES). To this end, the aforementioned equations are solved in a unified framework by equally treating the turbulent viscosity in both the RANS mode and the subgrid viscosity in the LES mode. It is also noted that, for IDDES, the subgrid length scale depends on not only local cell size but also the distance to the nearest wall. A shielding function is used to avoid deteriorating the detection of the boundary layer edge by excessively low subgrid viscosity, so that the boundary layer can be surely covered by the RANS model. Similar hybrid LES/RANS modeling has also been used in previous simulations of cavity assisted supersonic combustors fueled with hydrogen [21] and ethylene [22].

The filtered reaction-rate term $\overline{\dot{\omega}}_k$ accounting for the turbulence-combustion interaction is calculated by the multi-scale partially stirred reactor (PaSR) model [23]. In this model, $\overline{\dot{\omega}}_k$ is determined by the characteristic time scales for reaction (τ_c) in fine structure and micro-mixing in less reactive surroundings (τ_m) as

$$\overline{\dot{\omega}}_k = \frac{\tau_c}{\tau_c + \tau_m} \dot{\omega}_k(\overline{p}, \tilde{T}, \tilde{Y}_k) \quad (8)$$

where $\dot{\omega}_k(\overline{p}, \tilde{T}, \tilde{Y}_k)$ is the reaction rate based on the filtered flow quantities. The micro-mixing time scale is calculated as $\tau_m \sim (\nu_{eff}/\varepsilon)^{1/2}$, in which the effective viscosity $\nu_{eff} = \nu + \nu_t$ is the sum of the laminar and turbulent viscosities, and the dissipation rate can be related to the filtered strain rate tensor via $\varepsilon = k^{3/2}/\Delta$ and $k = (\upsilon_t \Delta/0.069)^2$, with Δ being the local grid size [24]. The chemical time scale in the present simulation is estimated as the ratio of the summation of species concentrations to that of the forward production rates, $\tau_c = \sum_{k=1}^{N_S} c_k / \sum_{k=1}^{N_S} \dot{\omega}_k^+$. The embedded multi-scale nature of the PaSR model makes it very suitable for intricate flame dynamics, and it has been fully confirmed in previous simulations regarding supersonic combustion [25,26] and high-speed jet flame [24].

To accurately describe the chemical kinetics, a detailed hydrogen/air mechanism consisting of 9 species and 19 reactions [27] is adopted in the present simulation. This mechanism was developed for wide ranges of pressure and equivalence ratio, which make it suitable for various hydrogen flames. Recently, five hydrogen oxidation chemistry mechanisms have been compared in a strut-injection supersonic combustor, in which the Burke et al.'s mechanism was found to more accurately agree with the experiment data [28]. Moreover, the reliability of the mechanism in supersonic combustion simulation has also been proven in denotation [29] and cavity stabilized combustor [25].

2.2.3. Numerical algorithm and solver

The numerical simulation was performed by using a home-developed code, a density-based solver for unsteady compressible reactive flows, which is based on the OpenFOAM's standard compressible solver rhoCentralFoam [30]. The main modifications are
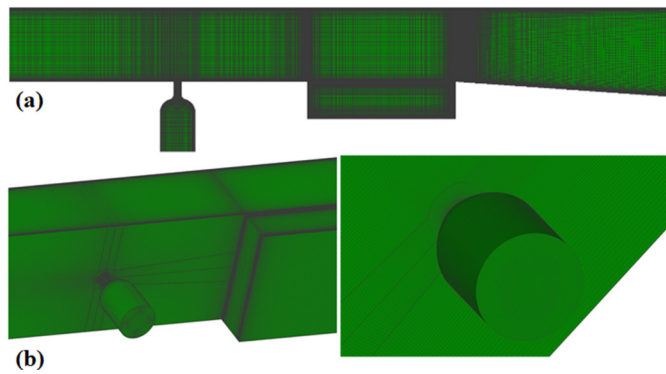
Fig. 3. Computational grid of the combustor (a) front view and (b) zoom-in view of the fuel injector.

Fig. 4. Scatter plot of μ_t/μ versus heat release rate colored by temperature. (For interpretation of the colors in the figure(s), the reader is referred to the web version of this article.)

to include multi-species transport and chemical reaction. The non-linear inviscid convective fluxes are constructed by the Kurgov-Tadmor scheme [31], which ensures a second-order dissipation in capturing discontinuities yet a high computational efficiency due to its Riemann-free simplicity. The diffusive fluxes are discretized by using central differencing, while time integration is advanced by the Crank-Nicholson scheme.

The solver has been validated in non-reactive cavity flow [32], highly under-expanded jet [33], and hydrogen-fueled supersonic combustion [34]. Furthermore, the present S-A model based ID-DES modeling methodology has also been cautiously validated in kerosene-fueled cavity combustors with both rectangular [35] and round-to-ellipse [36] cross sections.

2.3. Computational implementation

The computational domain schematized in Fig. 2 incorporates the isolator, combustion and expansion sections in their full scales. The block-structured hexahedral grid is generated with local re-finement imposed in the vicinity of the fuel jet and cavity shear layer. The fuel jet is resolved with refined grid sizes of 0.03 mm to 0.1 mm. The leading and trailing edges of the cavity, as well as the cavity shear layer are discretized with 0.03 mm grid to capture the destabilization of the shear layers. An inflation layer comprising 22 grids is deployed on the combustor wall as shown in Fig. 3(a). The first layer adjacent to the wall is about 5 μm, which corresponds to a non-dimensional cell size of $y^+ < 1$ on all the wall surfaces. The average thickness of the inflation layer is about 2.1 mm with the last cell still residing in the logarithm layer to ensure the valid-ity of the IDDES modeling. Since the instantaneous y^+ would vary both spatially and temporally, to prevent y^+ from extruding into the logarithmic layer, and extension of y^+-insensitive wall treat-ment is made to the standard S-A model by calculating the wall shear stress according to the log-law [35]. The total number of grid cells is 14.3 million, while a coarser grid of 7.2 million and a finer one of 27.9 million are used for grid convergence study.

Although the turbulence modeling methodology employed in the current simulation is IDDES, the main combustion region re-sembles a lifted jet flame since the inflow stagnation temperature is high enough to render a jet-wake flame stabilization mode. Con-sequently, the main chemically reactive region could be resolved with LES grid and reliably modeled by LES subgrid model. To this end, a *posteriori* analysis of the present mesh resolution is con-ducted in terms of the ratio of the SGS to molecular viscosities, μ_t/μ in the chemically reactive region where local heat release rate is no less than 1% of the global maximum one. As can be observed in Fig. 4 that most of the heat release and noticeable temperature rise concentrate in the region where μ_t/μ is pre-

dominately below 1.0, indicating that the LES is well resolved in the combustion region.
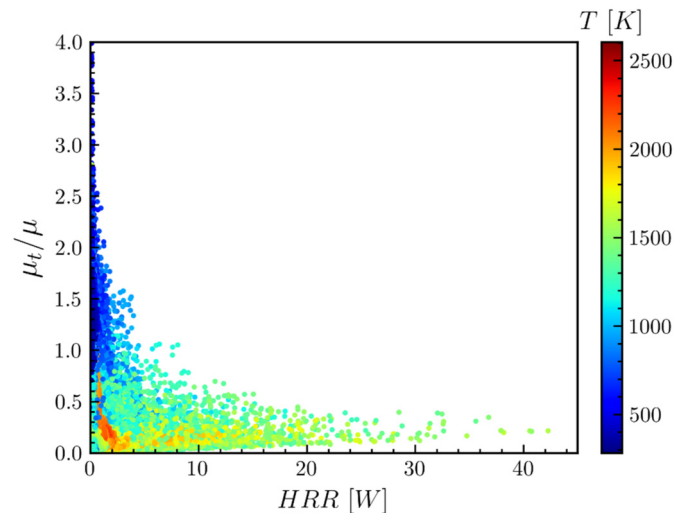
As for the boundary conditions, the air inlet is specified with static pressure, temperature and species composition, while the mean profile of the velocity is modulated by white noise with magnitude of 5%. A RANS-type turbulence boundary condition for viscosity is enforced at the air inlet as $\upsilon_t/\upsilon = 1$. To simulate a more realistic process of fuel injection, a sufficiently large tank is installed upstream the injector as in Fig. 3 (b), which is driven by total pressure and temperature. All the solid walls including the combustor and the fuel injection system are treated as non-slip boundaries. At the combustor exit, zero gradient conditions are imposed to all the flow variables. It is worth noting that for the cavity-assisted combustion, the simulation results may be sensi-tive to the wall thermal conditions. To mimic both the upper and lower limits for wall heat transfer, Micka [37] conducted a compar-ative numerical study for the same experiment condition as in the current work assuming an isothermal wall at 450 K and adiabatic wall and observed minor differences in the location and structure of flame stabilization. As a consequence, the adiabatic wall bound-ary was adopted in the present simulation since specific isothermal condition is not available for combustor under non-equilibrium thermal state.

The parallel computations are performed at the TianHe I su-percomputer clusters using 336 CPU cores. The time step is con-strained by a maximum Courant number of 0.3 to ensure nu-merical stability, thus resulting in a maximum time step around 1.5×10^{-9} s. The flow-through time for the combustor is estimated to be $t_f = L/U_\infty \approx 0.75$ ms. A typical simulation of $6t_f$ using the medium-scale grid of 14.3 million cells requires 0.55 million CPU hours, among which $2t_f$ are needed to reach the quasi-steady flow state followed by $4t_f$ for data sampling and statistics.

3. Results and discussion

3.1. Numerical validation

For a grid independence study, three topologically similar grids, such as 7.2 million, 14.3 million and 27.9 million, were used to predict the static pressures along the centerline of combustor's bottom wall. As shown in Fig. 5, the predicted static pressures for all the meshes are almost the same except at the cavity trailing edge location, where the medium and fine meshes predict higher
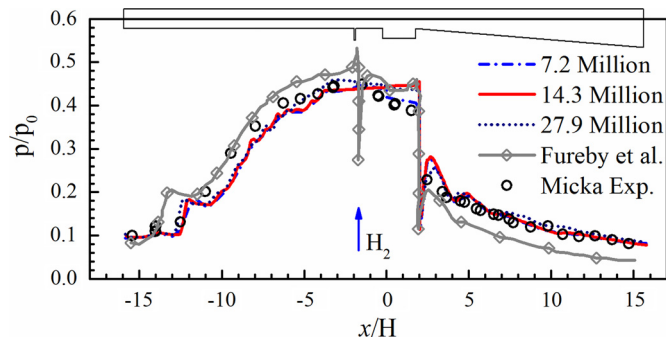
Fig. 5. Comparison of predicted static pressure distribution on the combustor bottom wall with Micka's experimental [37] and LES simulation result [13].
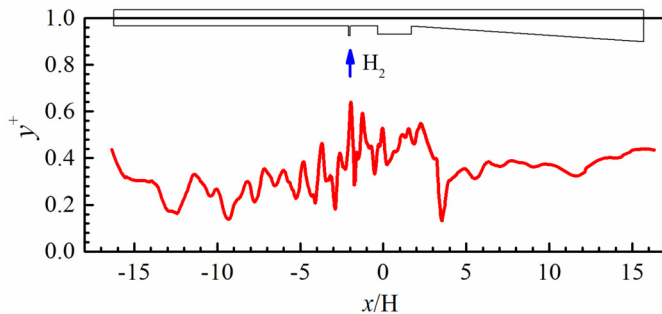
Fig. 6. Tim-averaged y^+ profile along the center line of the combustor's top wall.

pressure than does the coarse one. This may attribute to more intensive combustion on resolved scales due to local refinement. The maximum relative error between the medium and fine meshes is within 3%, which suggests the convergence of the grid resolution. To obtain a quantitative comparison between the computational results and experimental data, we interpolated the simulation prediction with the medium grid to where the pressure measurement exactly located. The average value of the relative error is around 8.7% which is acceptable for full-scale scramjet simulation. Thus the medium mesh was used to produce the results in the following sections, as a balance between numerical fidelity and computational efficiency.

Fig. 5 also shows Micka's experimental data and LES simulation by Fureby et al. [13] for comparison. It is seen that the present simulations with various grid resolutions satisfactorily reproduce the experimental observations on pressure trends: the pressure rise in the isolator (due to the shock-induced boundary layer separation), the pressure plateau towards the end of the isolator and along the cavity, and the abrupt depressurization immediately downstream the cavity rear. Fureby et al.'s LES simulation [13] employing a 7 species, 7 reactions hydrogen mechanism overpredicts the boundary layer separation point and the pressure in the isolator, but it underpredicts the pressure level downstream the cavity leading edge. Compared with Fureby et al.'s results, the better prediction of the present simulation may be attributed to the fact that the heat release rate distribution is accurately computed by using a better chemical kinetics so that the shock train in the isolator is accurately captured.

By definition, the non-dimensional wall distance y^+ depends not only on the grid size but also the local viscosity and velocity gradient, thus a post *priori* verification on the wall boundary layer resolution is necessary. Fig. 6 shows the streamwise variations of y^+ profile on the top wall for the medium-scale grid. It is seen that all y^+ values on combustor top wall are within 0.6. Around the fuel injection region, y^+ increases significantly as a result of flow separation induced by the fuel jet, but its maximum value is still within unity. Thus the aforementioned good agreement in the

magnitude and location of the pressure rise prediction may be also attributed to the adequate grid resolution near the walls.

Furthermore, away from the wall boundary layer, the dynamics of main flow especially its mixing between the fuel jet and entrainment by the cavity are resolved with local refined high fidelity LES grid. Fig. 7 presents the energy spectrum of the subgrid kinetic energy sampled at SP1 and SP2 with a fixed time interval of $\Delta t = 10^{-8}$ s, which are located in the jet wake region as denoted in Fig. 2. At both locations, the present simulation indicates the scaling law of $E(f) \sim f^{-8/3}$, rather than the exponent of $-5/3$ for incompressible flows (a detailed derivation is included in Appendix A). This suggests that the compressibility significantly affects the kinetic energy transfer from large to small scales [38]. A shorter inertial subrange is observed for the energy spectrum at location SP1, which is near the bottom wall and partially influenced by its confinement effect. Consequently, the turbulent mixing in the jet wake is believed to be well resolved in the present LES, which is prerequisite for the subsequent computational discoveries on the flame stabilization mechanism. Furthermore, as the turbulence statistical sampling frequency is about an order of magnitude larger than the CFD time step $\Delta t_{CFD} \sim 10^{-9}s$, the converging tendency of energy spectrum for $f > 10^7$ Hz in Fig. 7 should be attributed to this relatively low temporal resolution in data sampling.

3.2. Phenomenological description of flame stabilization

Fig. 8 shows perspective view of the isolator and combustor with side walls and isosurfaces of the vortex structures identified with Q criterion colored by static temperature. Since the local temperature in the region between the transverse fuel jet and the cavity is sufficiently high so that the hot combustion products remain in the fuel jet wake and above the cavity. The three-dimensional vortex structure is primarily initiated in the isolator by the shock-boundary-layer interaction. At the end portion of the combustor, the vortices are smeared out due to relatively coarse grid resolution.

The jet wake flame is further present in Fig. 9 for its Y_{OH} isosurface. It is clear that the production of OH radicals is initiated in the downstream vicinity of the fuel injector. The iso-surface of Y_{OH} mainly resides in between the fuel jet and the bottom wall. Hot products are then entrained into the cavity shear layer and subsequently mix and react with the fresh reactant mixture. It should also be noted that a large portion of OH radicals are accumulated above the rear part of the cavity. This indicates chain branching reactions favoring OH production are more intensive than that in the upstream locations.

To qualitatively validate the present simulation against the experiment for time-averaged OH* luminosity, as shown in Fig. 10(c), we noted that chemiluminescence could not be directly calculated. Consequently, we employed a model proposed by Mével et al. [39], which is based on the assumption that the chemiluminescence is originated from the $(A^2\Sigma^+ - X^2\Pi)$ transition of the excited hydroxyl radicals. The concentration of OH* is determined by the following three reactions: R1: $H + O + M = OH^* + M$; R2: $OH^* + M \Rightarrow OH + M$; R3: $OH^* \Rightarrow OH + h\nu$. Applying the quasi-steady-state-approximation (QSSA) to OH*, we have

$$[OH^*]_{QSSA} = \frac{k_1[H][O][M]}{(k_2 + k_{-1})[M] + k_3} \tag{9}$$

Fig. 10(a) shows the calculated $[OH^*]_{QSSA}$, which averages 100 successive snapshots sampled during $2t_f$. Spanwise superposition of the concentrations is performed to enable a direct comparison against the experiment by taking the line-of-sight nature of chemiluminescence into account. It can be seen that the overall behavior
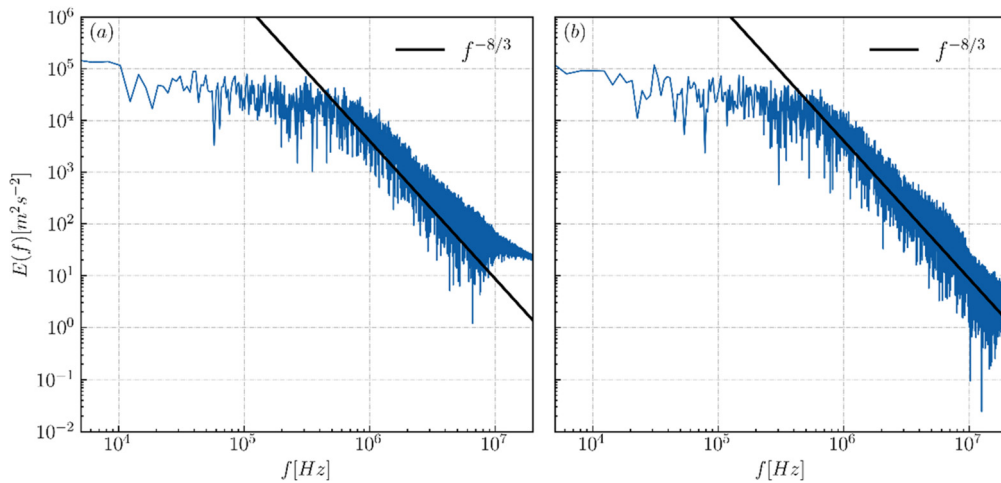
Fig. 7. Energy spectrum of k^{sgs} sampled at locations (a) SP1 and (b) SP2 as indicated in Fig. 2.
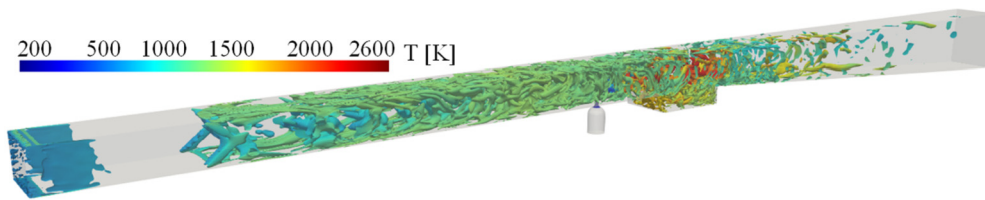
Fig. 8. Vortex structure characterized by Q criterion ($Q = 10^9 \ s^{-1}$) colored by the instantaneous temperature.
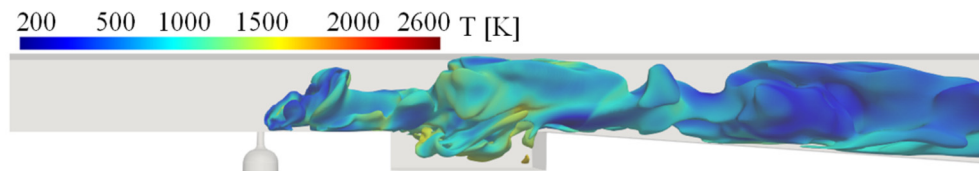
Fig. 9. Three dimensional rendering of Y_{OH} iso-surface colored by static temperature with $5 \times 10^{-3} < Y_{OH} < 2 \times 10^{-2}$.
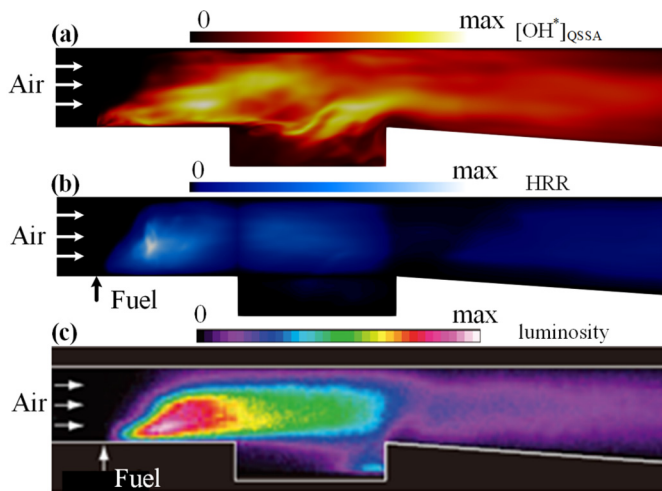
Fig. 10. (a) OH* luminosity, (b) heat release rate distribution predicted by numerical simulation, and (c) the experimentally measured OH* luminosity [37].

of the jet-wake flame mode is satisfactorily reproduced as such the reaction zone anchors itself a very short distance downstream of the fuel injection in the jet wake. The small discrepancy can be observed in the middle of the cavity; it may be attributed to the neglected cavity fuel injection at its rear wall, which has a negligible influence on the overall flame characteristics yet affects

the local flow characteristics and equivalence ratio in the cavity. Moreover, the fidelity of the present simulation is further substantiated by the fact that the heat release rate distribution from the simulation resembles the experimentally measured OH* luminosity as shown in Fig. 10(b). The numerical predicted heat release concentrated in the region between the fuel jet wake and the cavity leading edge, which agrees with the experimental observation.

3.3. Chemical kinetic characteristics of jet-wake flame stabilization

Fig. 11(a) shows the instantaneous numerical schlieren in which the shock train develops from the boundary layer separation induced by significant shock-wave-boundary layer interaction followed by large separation zones. In the further downstream, turbulence transition occurs with the breakdown of the core flow, resulting in a pressure plateau from $x/H = -6$ till the fuel injector, as illustrated in Fig. 5. At the injection location, variations in density gradient can be observed because of the presence of bow shock, the rapid change in density by hydrogen injection into the main flow, and the thermal expansion due to combustion in the vicinity of the cavity.

In Fig. 11(b), the instantaneous temperature gradually builds up in the isolator as the deceleration of the inflow by shock train system and significantly increases behind the fuel injector. The high-temperature regions in the fuel jet wake and above the cavity extend all the way to the cavity trailing edge, where intensive heat release occurs. In the meantime, the hot combustion products
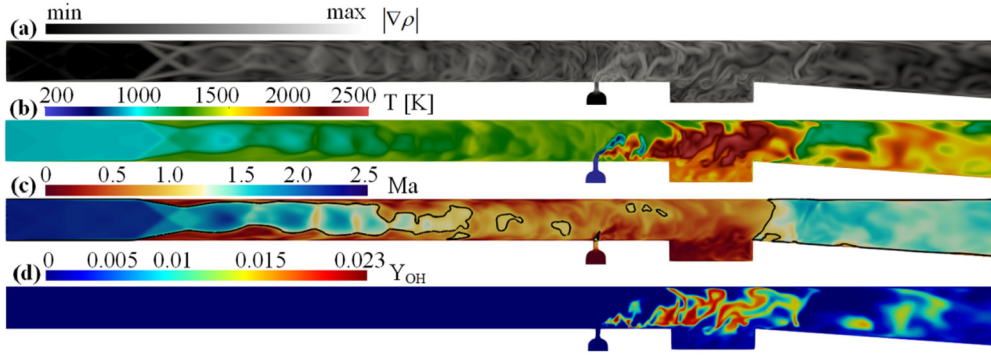
Fig. 11. Instantaneous flow fields showing (a) wave structures, (b) temperature, (c) Mach number, and (d) OH radical distribution on the combustor center plane.
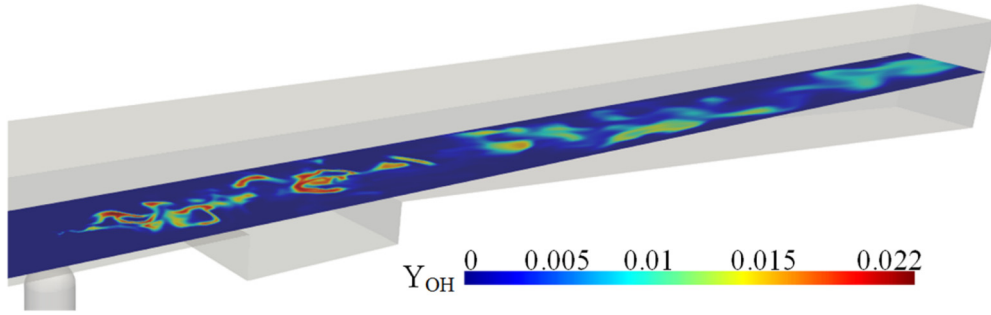
Fig. 12. Instantaneous OH mass fraction distribution on the lateral plane of Y=2 mm.

interact with the cavity shear layer and are entrained into the cavity. Furthermore, Fig. 11(c) exhibits the instantaneous Mach number distribution, embodying typical feature of dual-mode scramjet. The supersonic inflow first slows down in the isolator, becomes subsonic in its rear part and the entire cavity section, and then accelerates to supersonic again after a very short distance in the expansion section. It is noted that a thermal throat always locates at the cavity trailing edge.

Fig. 11(d) presents the contour of OH radicals on the combustor central plane, where the jet-wake flame mode can be easily recognized by a discernable amount of OH radicals. In the cavity section, most of the OH radicals reside above the cavity and only a negligible amount of them in the cavity. This finding is in accordance with the jet-wake flame stabilization mode in which the cavity effect in flame holding is secondary. In the downstream vicinity of the cavity rear, flame quenching is intensified with the rapid increase of flow velocity and the decrease of static temperature in the divergence section, manifested by the significant decrease of Y_{OH}. At further downstream locations, the partial resurgence of chemical reactions is the result of radical accumulation and interaction that require sufficient time to occur.

In the experiment of Micka and Driscoll [7], the flame luminosity is a line-of-sight integrated technique such that the side wall effect generally could not be precluded, as the flame can propagate upstream in the boundary layer along the side walls [40]. Thus, distribution of OH radicals on the lateral plane 2 mm above the bottom wall of the isolator is illustrated in Fig. 12. It can be seen that in the jet wake and cavity regions, the OH radicals distribute close to the combustor central plane, while they are more dispersed in the spanwise direction at further downstream locations. This finding substantiates the conclusion that the side wall effect is negligible in flame stabilization mode at the present combustor configuration.

3.4. Integral performance of dual-mode combustion

The quasi-one-dimensional (quasi-1D for short) analysis is widely used as a method for fast albeit simplified evaluation of the integral performance and initial phase design of scramjet engines. Recently, it was adopted by Yuan et al. [41] to reveal the dynamics of oscillating flame stabilization mode in ethylene fueled cavity supersonic combustor. In the present work, mass-weighted integration on the cross-section at each streamwise location is performed to obtain the quasi-1D distribution for corresponding physical property. To quantify the combustion performance, we defined the total pressure loss as

$$\eta_{p0}(x) = 1 - \frac{\int p_0(x)\rho \boldsymbol{u}(x) \cdot d\boldsymbol{S}}{\int p_0(0)\rho \boldsymbol{u}(0) \cdot d\boldsymbol{S}} \tag{10}$$

in which $\boldsymbol{u}$ denotes the velocity vector, $d\boldsymbol{S}$ the directional area of the cross-section, $p_0(x)$ is the total pressure at location x. Conventionally, combustion efficiency is defined based on the stable combustion product, namely H_2O in hydrogen/air combustion [42]. However, since water vapor is included in the vitiated air inflow, the combustion efficiency is reformulated by considering heat release:

$$\eta_{com}(x) = \frac{\int_0^x d\dot{Q}(x)\rho \boldsymbol{u}(x) \cdot d\boldsymbol{S}}{\dot{m}_{fuel}q_c} \tag{11}$$

where $d\dot{Q}(x)$ is the heat release rate at location x, $\dot{m}_{fuel}$ represents the fuel mass flow rate at the fuel injector, and q_c is the heat of combustion of hydrogen.

Quasi-1D distributions of Mach number and non-dimensional temperature $\hat{T} = T/T_{inlet}$ are shown in Fig. 13 (a) and (b). Starting from Ma=2.2 at the entrance of the isolator, Ma decreases along the isolator until it suddenly increases to sonic condition near the cavity trailing edge, then continues to increase gradually till the
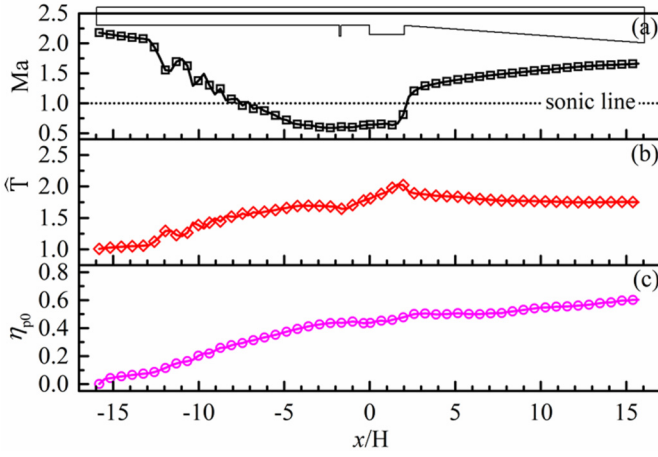
Fig. 13. Quasi-1D distribution of aerodynamic metrics (a) Mach number, (b) temperature and (c) total pressure loss.
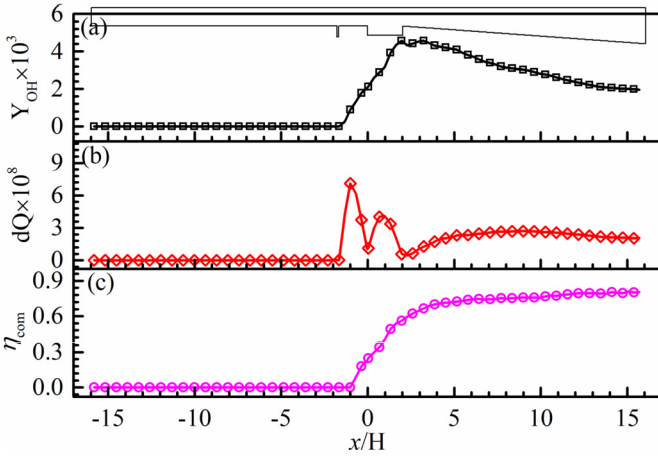
Fig. 14. Quasi-1D distribution of aerodynamic metrics (a) mass fraction of OH, (b) heat release rate and (c) combustion efficiency.

Fig. 15. (a) Flame structure shown in flame index, (b) HO$_2$ radial contour superposed with heat release rate dQ̇ indicated by white contour lines and (c) net production rate of the progress variable. The thick white lines in subfigures (a) and (c) represent stoichiometric mixture fraction.

combustor exit. Slight oscillations of Ma are discernable in the isolator and may be attributed to large separation zones induced by shock-boundary-layer interaction. The temperature profile gradually increases until the fuel injection, rises up steeply in the jet wake region, peaks at the cavity trailing edge, and slightly decreases in the expansion section eventually. As for the total pressure loss, it monotonically builds up till the combustor exit, no local overshot is observed in the jet wake region, which indicates that combustion-induced total pressure loss is secondary due to a relatively small overall equivalence ratio ($\phi_g = 0.24$).

Fig. 14 (a) presents the quasi-1D distribution of OH radical. It is seen that OH radical starts to build up from the location of fuel injection, which identifies the jet wake flame stabilization mode. Then the OH radicals continue to accumulate, and OH mass fraction reaches its peak value at the cavity trailing edge. Likewise, heat release rate bears an abrupt increase at the fuel injector. Two local minima can be observed at the leading and trailing edges of the cavity respectively, where combustor geometry changes suddenly. The combustion efficiency defined in Eqn. (11) is shown in Fig. 14(c). It increases quickly in the fuel jet wake region, indicating a majority of fuel completion till the trailing edge of the cavity.

3.5. Fluid-dynamical analysis of the flame stabilization

It has been hypothesized that the jet-wake flame stabilization was realized by auto-ignition [12]. However, this hypothesis

is based on the estimated auto-ignition delay time under homogeneous condition, and it does not consider fluid-dynamic and transport effects. To reveal the underlying physics of flame inhomogeneity, the Takeno flame index FI was defined as the normalized dot product of the gradients of the fuel and oxidizer mass fractions $\nabla Y_{H2} \cdot \nabla Y_{O2}/(|\nabla Y_{H2}| \cdot |\nabla Y_{O2}|)$ denotes premixed flame with FI= +1 and non-premixed with FI=-1 [43,44], as shown in Fig. 15(a). We also note that there are other sophisticated diagnostic tools for flame index such as those proposed by Buttay et al. [45] and Illana et al. [46], the Takeno index is employed in the present study for its simplicity. Since the flame index is unable to distinctly delimit the non-premixed combustion from pure mixing, the heat release is also shown in Fig. 15(b). It can be seen that pure mixing between the fuel and oxidizer is dominant on the windward side of the jet plume because no heat release occurs there. Premixed flames emerge on the leeward side of the jet plume, in which the HO$_2$ radical is in a considerable concentration indicating strong reactivity with intensive heat release. A discernable amount of heat release from non-premixed combustion also can be observed in the leeward side of the fuel jet and evidences the interlaced premixed flame and non-premixed combustion in this region (interlaced region). This is a consequence of the shrunken induction region I and upstream moved region II in Micka et al. [12], as discussed in the Introduction section. In further downstream, as the disintegration of jet plume, the turbulent non-premixed region takes over the dominancy in flame stabilization, as indicated in Fig. 15(a) and will be further discussed below.

To quantify the effect of auto-ignition, normalized progress variable is defined as $c = \psi/\psi_{eq}$, where $\psi = Y_{H_2O}$ and ψ_{eq} is the equilibrium H_2O mass fraction for the local mixture [47]. The corresponding governing equation for the normalized progress variable reads [48]

$$\overline{\rho}\frac{D\tilde{c}}{Dt} = \nabla \cdot \left[(\mathcal{D} + \mathcal{D}_t)\nabla\tilde{c}\right] + \overline{\dot{\omega}}_c^* \tag{12}$$

where $D(\cdot)/Dt$ denotes the substantial derivative, while $\mathcal{D}$ and $\mathcal{D}_t$ represent the molecular and turbulent mass diffusivity, respectively. As in Fig. 15(c), the source term $\overline{\dot{\omega}}_c^*$ shows that auto-ignition event embodies discrete regions, which is ectopic from the premixed flame sheets denoted by the bright yellow patches. This
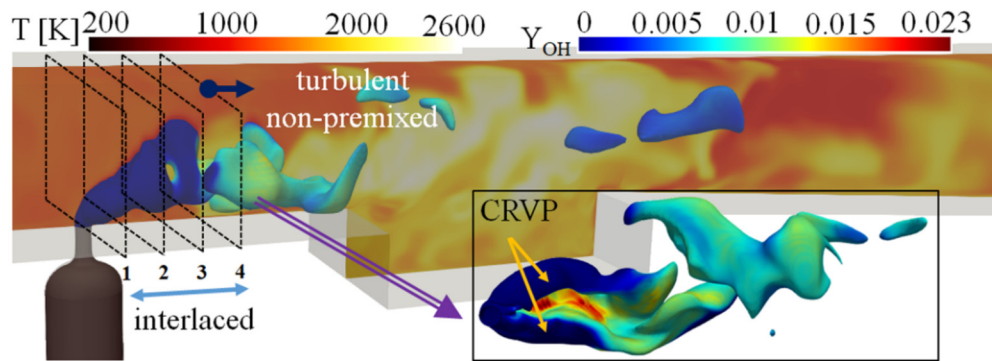
Fig. 16. Zoom-in view of the leeward side of the fuel jet in which the iso-surface of hydrogen is rendered by Y_{OH}.
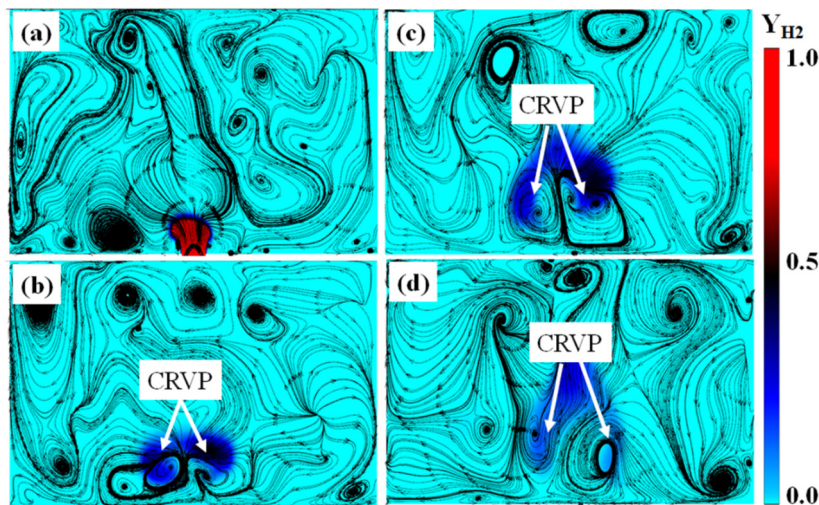
Fig. 17. Instantaneous contour of Y_{OH} superposed with streamline (a) at location 1 (cutting through the middle plane of the injector), (b) at location 2, (c) at location 3 and (d) at location 4.

observation further substantiates that the flame stabilization is firstly initiated by premixed flame in the leeward side of the jet plume (region I), while auto-ignition becomes remarkable in the interlaced region (region II) and takes dominancy in further downstream locations.

To further scrutinize the flame structure in the jet-wake mode, a zoom-in view of the fuel jet shown in Fig. 16. The fuel jet is visualized by Y_{H2} iso-surface and colored by Y_{OH}. This configuration resembles the well-understood canonical jet in supersonic cross flow (JISC) [8], which indicates that the fuel injection and mixing downstream the injector are dominantly controlled by the counter-rotating vortex pair (CRVP) along the trajectory of the H_2 plume. The Kelvin-Helmholtz instability develops on the jet shear-layer and wrinkles the windward side of the fuel plume. Further downstream, the H_2 plume becomes fragmented and shrunken due to the combustion depletion. Different from the typical JISC, the fuel plume has no bow-shock or obvious recirculation zone in its upstream because the local flow is subsonic. Consequently, the strain rate on the windward side is not high enough for fuel-oxidizer mixing, which also hinders subsequent combustion on the windward side of the jet plume. The reaction zone in leeward side of the jet plume was previously observed in reacting flow of premixed jet in hot crossflow [49], but its role in non-premixed flame stabilization in supersonic combustion has not been reported.

Fig. 17 further resolves the local flow characteristics on the leeward side of the jet by visualizing the streamlines at four streamwise locations as denoted in Fig. 16. On the first plane which vertically cuts through the injector hole as shown in Fig. 17(a),

mixing takes place between the fuel and the free-stream in the jet periphery. On the plane presented in Fig. 17(b), $2D$ away from the fuel injector, a CRVP appears due to the obstruction effect of the cross flow on the jet fluid. This CRVP then grows in further downstream as shown in Fig. 17(c) and (d), and it provides a major arena where fuel/air mixing occurs. It is noted that the CRVP remarkably promotes the mixing while reduces the local flow velocity on the leeward side of the jet plume, which are required for the formation of premixed flames. Thus the premixed flames serve as "pilot flame" to sustain subsequent non-premixed combustion in the downstream. This coincides with the observations shown in Fig. 11(d) and Fig. 16 that combustion emerges in the leeward side instead of the windward side.

3.6. Transport and kinetics of radicals in vortical jet-wake flow

It is of interest to investigate the role of vortical jet-wake flow in affecting the transport and kinetics of radicals. Fig. 18 shows the distributions of Y_{OH} and $d\dot{Q}$ in mixture fraction (Z) space, with data sampled from streamwise planes at locations 2-4, whose normal distances to the center of the injector are 2D, 4D and 6D, respectively. At location 2, both OH radicals and heat release produced by premixed flame and non-premixed combustion are comparable whereas the former spans over a wide range of mixture fraction while the latter concentrates more around Z_{st}. In Fig. 18(c) and (d), OH radicals and heat released associated with premixed flame decrease gradually and shift to fuel rich regime. At location 4, non-premixed combustion dominates the radical and heat production
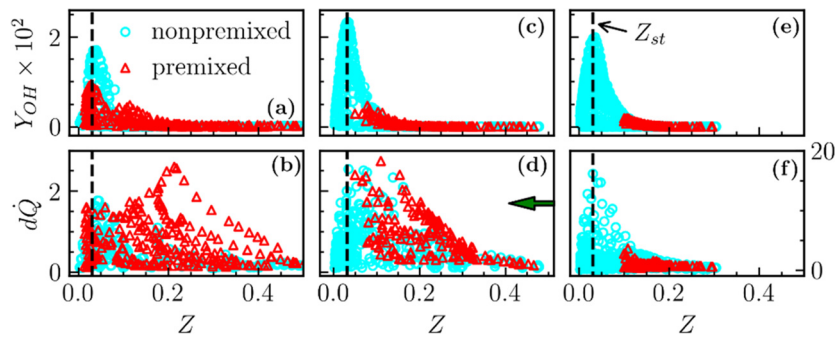
Fig. 18. Distributions of Y_{OH} and $d\dot{Q}$ in mixture fraction space at three streamwise locations whose normal distance to the center of the injector are: 2D (location 2, a-b), 4D (location 3, c-d) and 6D (location 4, e-f).
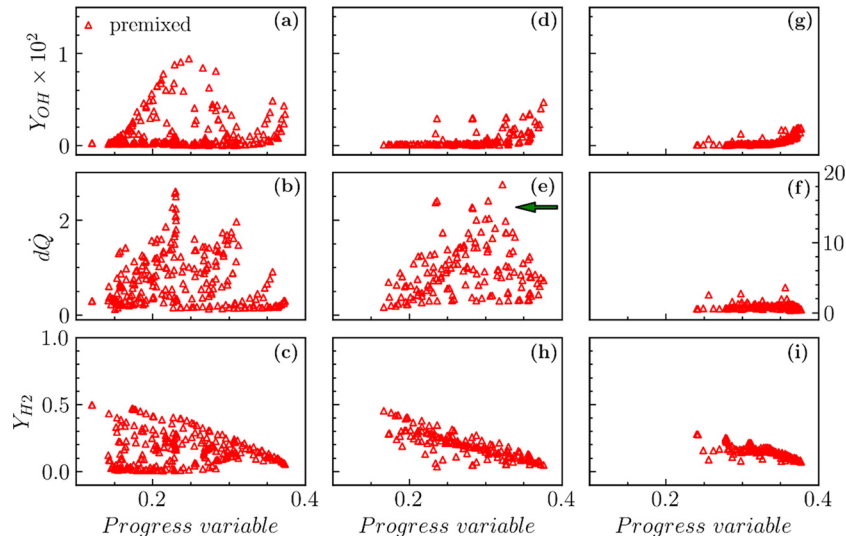
Fig. 19. Scatters of OH mass fraction and heat release of premixed mode versus progress variable at three streamwise locations whose normal distance to the center of the injector are: 2D (location 2, a-c), 4D (location 3, d-h) and 6D (location 4, g-i).

since premixed flames cannot be sustained due to the disintegration of the jet plume and combustion depletion.

To characterize the degree to which the chemical reactions proceed in premixed combustion mode, the produced H_2O is chosen as the progress variable to plot the reactive scalars and the heat release rate at three typical locations. As shown in Fig. 19, Y_{H2} decreases with the progress variable at all the locations, but the fuel depletion in the upstream location (location 2) is more susceptible to turbulent unsteadiness in the jet wake. The heat release rate and Y_{OH} first increases from zero and then decreases to zero at location 2, with their maximum values appearing near the stoichiometric mixture fraction. A high turbulence intensity dissipates the chemical heat release in the unsteady jet wake flow, accompanied by the farming of OH radical pool. This further substantiates the fact that the premixed flame portion in the jet wake is indispensable for flame stabilization at downstream locations.

4. Concluding remarks

This study investigates the jet-wake flame stabilization mechanism of a hydrogen-fueled dual-mode scramjet using finite-chemistry hybrid LES/RANS simulation with 9-species and 19 steps detailed hydrogen oxidation mechanism. The simulated condition corresponds to the experiment by Micka et al. [7,37] featuring room temperature hydrogen injection into hot cross flow at 1400 K. The present simulation satisfactorily reproduced this flame stabilization mode in terms of the qualitative OH* luminosity and the quantitative wall pressure measurements.

Analyses of the three-dimensional flow characteristics, flame structure, and mixture fraction show that the jet-wake flame can be divided into two regions: the interlaced region and the turbulent non-premixed combustion region, simpler than the three-region division in Micka and Driscoll [12] for H_2/C_2H_4 mixture combustion. The first region resides in the leeward side of the fuel jet wake, where both premixed flames and non-premixed combustion contribute to the OH radicals' production whereas more heat release is associated with the premixed flame portion. Moreover, the non-premixed combustion portion concentrates around Z_{st} while premixed flames occur in a much wider mixture fraction space. Further downstream, as the fuel jet plume breaks down and is consumed by combustion, turbulent non-premixed combustion becomes dominant.

The rationality of the presence of premixed flames in the interlaced region is further revealed by three-dimensional features of the complex reacting flow. The premixed flames are located in the leeward side of the fuel jet and mainly sustained by the counter-rotating vortex pair, which enhances local mixing and reduces flow velocity. The premixed flames play the role of "pilot flame" for downstream turbulent non-premixed combustion, which takes place in the leeward periphery of the fuel jet. With the in-depth understanding of the jet-wake flame stabilization gained in the present study, other flame stabilization modes such as cavity and oscillation modes will be investigated in our future work. Furthermore, the influence of the chemical reactivity of hydrocarbon fuel in flame stabilization is also worthy of further efforts.

Declaration of competing interest

The authors declare that they have no known competing financial interests or personal relationships that could have appeared to influence the work reported in this paper.

Acknowledgement

Appendix A

The functional dependence of the energy spectrum in supersonic flows is derived by means of dimensional analysis. In supersonic flows, the turbulent kinetic energy density per unit wave number, E, depends on the wave number k, the rate of energy dissipation per unit volume ε, and the flow density, now is involved in as an independent variable.

$$k = L^{-1} \tag{A.1}$$

$$\varepsilon = ML^2T^{-3} \tag{A.2}$$

$$\rho = ML^{-3} \tag{A.3}$$

$$E = ML^3T^{-2} \tag{A.4}$$

Assuming that E depends on k, ρ and ε, the energy density per unit wave number is $E(k, \rho, \varepsilon)$ and should be expressed as $Ck^\alpha \rho^\beta \varepsilon^\gamma$, where C is a constant. Subsequently, the exponents α, β and γ are determined to be $-8/3$, $2/3$ and $1/3$, respectively. Thus, with the previous assumption:

$$E(k, \rho, \varepsilon) = Ck^{-8/3}\rho^{1/3}\varepsilon^{2/3} \tag{A.5}$$

whereas in subsonic incompressible flows, $E(k, \varepsilon) = Ck^{-5/3}\varepsilon^{2/3}$.

References

[1] J. Urzay, Supersonic combustion in air-breathing propulsion systems for hypersonic flight, Annu. Rev. Fluid Mech. 50 (1) (2018) 593–627.

[2] M. Gamba, M.G. Mungal, Ignition, flame structure and near-wall burning in transverse hydrogen jets in supersonic crossflow, J. Fluid Mech. 780 (2015) 226–273.

[3] J. Zhang, J. Chang, Z.a. Wang, L. Gao, W. Bao, Flame propagation and flashback characteristics in a kerosene fueled supersonic combustor equipped with strut/wall combined fuel injectors, Aerosp. Sci. Technol. 93 (2019) 105303.

[4] B. An, M. Sun, Z. Wang, J. Chen, Cavity flameholding subjected to an expansion fan in a rocket-based combined cycle combustor, Aerosp. Sci. Technol. 106 (2020) 106180.

[5] F. Zhong, L. Cheng, H. Gu, X. Zhang, Experimental study of flame characteristics of ethylene and its mixture with methane and hydrogen in supersonic combustor, Aerosp. Sci. Technol. 86 (2019) 775–781.

[6] A. Ben-Yakar, R.K. Hanson, Cavity flame-holders for ignition and flame stabilization in scramjets: an overview, J. Propuls. Power 17 (4) (2001) 869–877.

[7] D.J. Micka, J.F. Driscoll, Combustion characteristics of a dual-mode scramjet combustor with cavity flameholder, Proc. Combust. Inst. 32 (2) (2009) 2397–2404.

[8] K. Mahesh, The interaction of jets with crossflow, Annu. Rev. Fluid Mech. 45 (1) (2013) 379–407.

[9] E.F. Hasselbrink, M.G. Mungal, Transverse jets and jet flames. Part 2. Velocity and OH field imaging, J. Fluid Mech. 443 (2001) 27–68.

[10] D. Han, M.G. Mungal, Simultaneous measurements of velocity and CH distribution. Part II: deflected jet flames, Combust. Flame 133 (1–2) (2003) 1–17.

[11] A. Ben-Yakar, M.G. Mungal, R.K. Hanson, Time evolution and mixing characteristics of hydrogen and ethylene transverse jets in supersonic crossflows, Phys. Fluids 18 (2) (2006) 026101.

[12] D.J. Micka, J.F. Driscoll, Stratified jet flames in a heated (1390 K) air cross-flow with autoignition, Combust. Flame 159 (3) (2012) 1205–1214.

[13] C. Fureby, J. Tegnér, R. Farinaccio, R. Stowe, D. Alexander, A computational study of a dual-mode ramjet combustor with a cavity flameholder, Int. J. Energ. Mater., Chem. Propuls. 11 (6) (2012) 487–510.

[14] H. Koo, P. Donde, V. Raman, A quadrature-based LES/transported probability density function approach for modeling supersonic combustion, Proc. Combust. Inst. 33 (2) (2011) 2203–2210.

[15] M.W. Chase, JANAF thermochemical tables, J. Phys. Chem. Ref. Data 3 (2) (1974) 311–480.

[16] S. Arvidson, L. Davidson, S.-H. Peng, Hybrid Reynolds-averaged Navier–Stokes/large-eddy simulation modeling based on a low-Reynolds-number k-ω model, AIAA J. 54 (12) (2016) 4032–4037.

[17] Z. Wu, Z. Gao, C. Jiang, C. Lee, An in-depth numerical investigation of a supersonic cavity-ramp flow with DDES method, Aerosp. Sci. Technol. 89 (2019) 253–263.

[18] A. Saghafian, L. Shunn, D.A. Philips, F. Ham, Large eddy simulations of the HIFiRE scramjet using a compressible flamelet/progress variable approach, Proc. Combust. Inst. 35 (2) (2015) 2163–2172.

[19] P. Spalart, S. Allmaras, A one-equation turbulence model for aerodynamic flows, in: 30th Aerospace Sciences Meeting and Exhibit, Reno, NV, USA, 1992.

[20] M.L. Shur, P.R. Spalart, M.K. Strelets, A.K. Travin, A hybrid RANS-LES approach with delayed-DES and wall-modelled LES capabilities, Int. J. Heat Fluid Flow 29 (6) (2008) 1638–1649.

[21] J.-Y. Choi, F. Ma, V. Yang, Combustion oscillations in a scramjet engine combustor with transverse fuel injection, Proc. Combust. Inst. 30 (2) (2005) 2851–2858.

[22] P. Cocks, J. Donohue, C. Bruno, M. Haas, IDDES of a dual-mode ethylene fueled cavity flameholder with an isolator shock train, in: 51st AIAA Aerospace Sciences Meeting Including the New Horizons Forum and Aerospace Exposition, Grapevine, Texas, 2013.

[23] A. Karlsson, Modeling Auto-Ignition, Flame Propagation and Combustion in Non-stationary Turbulent Sprays, Chalmers University of Technology, Göteborg, Sweden, 1995.

[24] Y. Moule, V. Sabelnikov, A. Mura, Highly resolved numerical simulation of combustion in supersonic hydrogen–air coflowing jets, Combust. Flame 161 (10) (2014) 2647–2668.

[25] J.A. Fulton, J.R. Edwards, A. Cutler, J. McDaniel, C. Goyne, Turbulence/chemistry interactions in a ramp-stabilized supersonic hydrogen–air diffusion flame, Combust. Flame 174 (2016) 152–165.

[26] K. Nordin-Bates, C. Fureby, S. Karl, K. Hannemann, Understanding scramjet combustion using LES of the HyShot II combustor, Proc. Combust. Inst. 36 (2) (2017) 2893–2900.

[27] M.P. Burke, M. Chaos, Y. Ju, F.L. Dryer, S.J. Klippenstein, Comprehensive H2/O2 kinetic model for high-pressure combustion, Int. J. Chem. Kinet. 44 (7) (2011) 444–474.

[28] B. Liu, G. He, F. Qin, J. An, S. Wang, L. Shi, Investigation of influence of detailed chemical kinetics mechanisms for hydrogen on supersonic combustion using large eddy simulation, Int. J. Hydrog. Energy 44 (10) (2019) 5007–5019.

[29] L. Shi, H. Shen, P. Zhang, D. Zhang, C. Wen, Assessment of vibrational non-equilibrium effect on detonation cell size, Combust. Sci. Technol. 189 (5) (2017) 841–853.

[30] C.J. Greenshields, H.G. Weller, L. Gasparini, J.M. Reese, Implementation of semi-discrete, non-staggered central schemes in a colocated, polyhedral, finite volume framework, for high-speed viscous flows, Int. J. Numer. Methods Fluids 63 (2009) 1–21.

[31] A. Kurganov, E. Tadmor, New high-resolution central schemes for nonlinear conservation laws and convection–diffusion equations, J. Comput. Phys. 160 (1) (2000) 241–282.

[32] Y. Lee, W. Yao, X. Fan, Low-dissipative hybrid compressible solver designed for large-eddy simulation of supersonic turbulent flows, AIAA J. 56 (8) (2018) 3086–3096.

[33] X. Li, W. Yao, X. Fan, Large-eddy simulation of time evolution and instability of highly underexpanded sonic jets, AIAA J. 54 (10) (2016) 3191–3211.

[34] K. Wu, P. Zhang, W. Yao, X. Fan, Computational realization of multiple flame stabilization modes in DLR strut-injection hydrogen supersonic combustor, Proc. Combust. Inst. 37 (3) (2019) 3685–3692.

[35] W. Yao, Y. Lu, K. Wu, J. Wang, X. Fan, Modeling analysis of an actively cooled scramjet combustor under different kerosene/air ratios, J. Propuls. Power 34 (4) (2018) 975–991.

[36] W. Yao, Y. Yuan, X. Li, J. Wang, K. Wu, X. Fan, Comparative study of elliptic and round scramjet combustors fueled by RP-3, J. Propuls. Power 34 (3) (2018) 772–786.

[37] D.J. Micka, Combustion Stabilization, Structure, and Spreading in a Laboratory Dual-Mode Scramjet Combustor, The University of Michigan, Ann Arbor, USA, 2010.

[38] A. Ingenito, C. Bruno, Physics and regimes of supersonic combustion, AIAA J. 48 (3) (2010) 515–525.

[39] R. Mével, S. Pichon, L. Catoire, N. Chaumeix, C.E. Paillard, J.E. Shepherd, Dynamics of excited hydroxyl radicals in hydrogen-based mixtures behind reflected shock waves, Proc. Combust. Inst. 34 (1) (2013) 677–684.

[40] T. Mathur, M. Gruber, K. Jackson, J. Donbar, W. Donaldson, T. Jackson, F. Billig, Supersonic combustion experiments with a cavity-based fuel injector, J. Propuls. Power 17 (6) (2001) 1305–1312.

[41] Y. Yuan, T. Zhang, W. Yao, X. Fan, P. Zhang, Characterization of flame stabilization modes in an ethylene-fueled supersonic combustor using time-resolved CH* chemiluminescence, Proc. Combust. Inst. 36 (2) (2017) 2919–2925.

[42] K. Kannaiyan, Numerical investigation of the local and global supersonic combustion characteristics of ethylene fuel, Aerosp. Sci. Technol. 106 (2020) 106178.

[43] H. Yamashita, M. Shimada, T. Takeno, A numerical study on flame stability at the transition point of jet diffusion flames, Symp., Int., Combust. 26 (1) (1996) 27–34.

[44] D.A. Rosenberg, P.M. Allison, J.F. Driscoll, Flame index and its statistical properties measured to understand partially premixed turbulent combustion, Combust. Flame 162 (7) (2015) 2808–2822.

[45] R. Buttay, L. Gomet, G. Lehnasch, A. Mura, Highly resolved numerical simulation of combustion downstream of a rocket engine igniter, Shock Waves 27 (4) (2017) 655–674.

[46] E. Illana, D. Mira, A. Mura, An extended flame index partitioning for partially premixed combustion, Combust. Theory Model. 25 (1) (2020) 121–157.

[47] Z. Chen, S. Ruan, N. Swaminathan, Simulation of turbulent lifted methane jet flames: effects of air-dilution and transient flame propagation, Combust. Flame 162 (3) (2015) 703–716.

[48] Z.X. Chen, I. Langella, N. Swaminathan, M. Stöhr, W. Meier, H. Kolla, Large eddy simulation of a dual swirl gas turbine combustor: flame/flow structures and stabilisation under thermoacoustically stable and unstable conditions, Combust. Flame 203 (2019) 279–300.

[49] O. Schulz, E. Piccoli, A. Felden, G. Staffelbach, N. Noiray, Autoignition-cascade in the windward mixing layer of a premixed jet in hot vitiated crossflow, Combust. Flame 201 (2019) 215–233.